

# Sulfur Polymers as Flexible Interfacial Additives for Low Stack-Pressure Solid-State Lithium-Ion Batteries

Trevor R. Martin,<sup>\*[a]</sup> Glenn Teeter,<sup>[a]</sup> Chun-Sheng Jiang,<sup>[a]</sup> and Kyusung Park<sup>[a]</sup>

Solid-state batteries (SSBs) fabricated using sulfide solid electrolytes (SSEs) typically require cell stackpressures in the range of tens to hundreds of megapascals to maintain effective interfacial contact and lithium-ion mobility across the full cell stack. These relatively high cell stackpressures necessarily require additional cell components that reduce the delivered volumetric and gravimetric capacities of SSBs. This work has developed a novel sulfur polymer (polyS) that improves lithium-ion conductivity in SSBs at low cell stackpressures, thereby directly targeting this technological limitation. Specifically, this work shows that polyS can be combined with the argyrodite

$\text{Li}_6\text{PS}_5\text{Cl}$  (LPSC) to form a stable composite SSE. By combining LPSC particles with a flexible additive that enhances interfacial contact at low pressures, this new polyS LPSC composite SSE material greatly improves ionic conductivity at cell stackpressures below 2.0 MPa in comparison to conventional LPSC composites. Furthermore, this polyS LPSC composite can be used to fabricate a full SSB that cycles reversibly at only 1.6 MPa. Finally, this composite SSE exhibits self-healing behavior when combined with a lithium metal electrode, wherein lithium dendrites are oxidized to form passivating  $\text{Li}_2\text{S}$  species that recover the cell from shorting.

## Introduction

Solid-state batteries (SSBs) offer a promising new route to fabricate high-capacity batteries by combining energy dense lithium metal anodes,<sup>[1]</sup> lithium-ion alloying materials,<sup>[2]</sup> conversion electrodes,<sup>[3]</sup> or lithium-air batteries<sup>[4]</sup> with a solid lithium-ion conducting material instead of a liquid electrolyte.<sup>[5–8]</sup> However, when compared to traditional liquid electrolyte cells, SSBs typically require both high initial pressure densification steps and extremely high cell stackpressures in the range of tens or several hundred MPa to ensure optimal ionic conductivity and effective interfacial contact between solid electrolyte particles and the electrode active materials.<sup>[1,2,5]</sup> To ensure that these high pressures are maintained during prolonged cell cycling, commercialized SSBs will require additional external confinement and pressurization components. This additional cell packaging will necessarily reduce the ultimate energy density gains that can be achieved with SSBs. Therefore, decreasing the required pressures for cell cycling is essential for SSB technological improvement.

Within the range of readily available solid electrolyte (SE) materials, the sulfide-based argyrodite  $\text{Li}_6\text{PS}_5\text{Cl}$  (LPSC) has emerged as a promising SE candidate due to its relatively high ionic conductivity at room temperature.<sup>[8]</sup> LPSC has been used to effectively fabricate cells with lithium metal electrodes.<sup>[1]</sup> However, sulfide-based solid electrolytes (SSEs) are prone to shorting via the formation of lithium metal dendrites and often will undergo pronounced interfacial redox reactions when

placed in contact with lithium metal electrodes.<sup>[1,7]</sup> To date, studies have addressed these issues using various interfacial coatings and passivation layers.<sup>[1,7,9]</sup>

Solid polymer electrolytes (SPEs) have been studied extensively during the previous decades; however research has been primarily focused on conventional polymeric structures wherein chains of carbon atoms comprise the polymeric backbone.<sup>[5,10]</sup> Previous reports have demonstrated that elemental sulfur can be reacted with vinylic aromatic compounds to form high-stability sulfur cathodes for lithium–sulfur batteries.<sup>[11–13]</sup> Subsequent publications leveraged this chemistry wherein sulfur radicals are reacted with various vinylic compounds to form new materials for a variety of applications including nanoparticle synthesis,<sup>[14]</sup> energy storage,<sup>[12,15,16]</sup> and optical applications.<sup>[17,18]</sup> Crystallographic analysis of various SSEs has revealed that  $\text{Li}^+$  ions typically coordinate near tetrahedrally arranged sulfur atoms to form a structure that facilitates the mobility of  $\text{Li}^+$  ions.<sup>[8]</sup> Using these discoveries as a starting point, we hypothesized that a soft and mechanically flexible sulfur polymer could be synthesized to form a new class of lithium-ion conducting polymers, wherein lithium atoms can coordinate with sulfur atoms as well as other nucleophilic organic moieties such as amines. Furthermore, we hypothesized that such a polymer could be used to improve ionic transport at low cell stackpressures.

Additional studies have shown that LPSC SE separator layers must be combined with chemically inert polymeric binders such as polyisobutene (polyIB) and must be processed in non-polar solvents to avoid LPSC degradation.<sup>[19,20]</sup> Herein we synthesize a novel ionically conductive sulfur polymer (polyS) with dimethylvinylbenzylamine (DMVBA), elemental sulfur, and lithium chloride. We demonstrate that this polyS material exhibits  $\text{Li}^+$  conductivities in the range of  $1 \mu\text{S}/\text{cm}$  at  $50^\circ\text{C}$ . Furthermore, since this polyS material is soluble in non-polar solvents such as toluene, we show that it can be combined with

[a] Dr. T. R. Martin, Dr. G. Teeter, Dr. C.-S. Jiang, Dr. K. Park  
Chemistry and Nanoscience Center, National Renewable Energy Laboratory,  
Golden, CO, 80401, USA  
E-mail: trevor.martin@nrel.gov

 Supporting information for this article is available on the WWW under  
<https://doi.org/10.1002/batt.202300255>

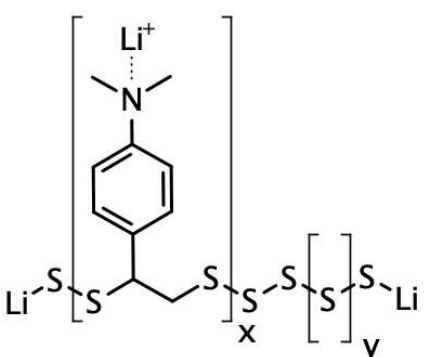
LPSC to form an effective SE composite material. We also show that this polyS LPSC composite operates as a flexible, ionically conductive interfacial layer that improves ionic conductivity at pressures below 2.0 MPa in comparison to a conventional polyIB LPSC composite. We also demonstrate that this polyS LPSC composite can be used to cycle a SSB with a lithium cobalt oxide (LCO) cathode and a graphite anode at the relatively low cell stack-pressure of 1.6 MPa. We show that in the polyS LPSC composite the LPSC grains are surrounded by comparatively soft polyS regions using atomic force microscopy (AFM) with contact resonance (CR) analysis. We also probe the interfacial evolution of the polyS LPSC composite during lithium plating using virtual electrode x-ray photoelectron spectroscopy (VE-XPS). Finally, we posit that the polyS imbues the SE

composite with self-healing properties when cycled in contact with a lithium metal electrode.

## Results and Discussion

We utilized the ring-opening radical polymerization of elemental sulfur with vinylic organic compounds to first polymerize elemental sulfur with DMVBA. Next, we reacted this polymer with lithium chloride in *n*-methyl-2-pyrrolidone (NMP). Scheme 1 depicts the molecular structure of the final sulfur polymer (polyS) used in this study, with a nominal x:y ratio that yields approximately 2 sulfur atoms to every 1 DMVBA monomer. Proton nuclear magnetic resonance (<sup>1</sup>H NMR) spectroscopy, Fourier transform infrared (FTIR) spectroscopy, and X-ray photoelectron spectroscopy (XPS) data for a polyS film are shown in Figures S1, S2, and S3, respectively. The spectra indicate the presence of all the predicted atomic species and confirm the general proposed structure illustrated in Scheme 1.

Next, we analyzed the ionic conductivity of a traditional polyIB LPSC composite, of a polyS LPSC composite, and of the polyS material by fabricating a thin film of each in contact with symmetric indium metal electrodes. Figure 1(a) shows a series of Nyquist plots depicting the temperature-dependent electrochemical impedance spectroscopy (EIS) data for a baseline composite solid electrolyte layer comprised of Li<sub>6</sub>PS<sub>5</sub>Cl (LPSC) argyrodite (90% by mass) and polyisobutene (polyIB) polymer



Scheme 1. Proposed general sulfur polymer (polyS) molecular structure.

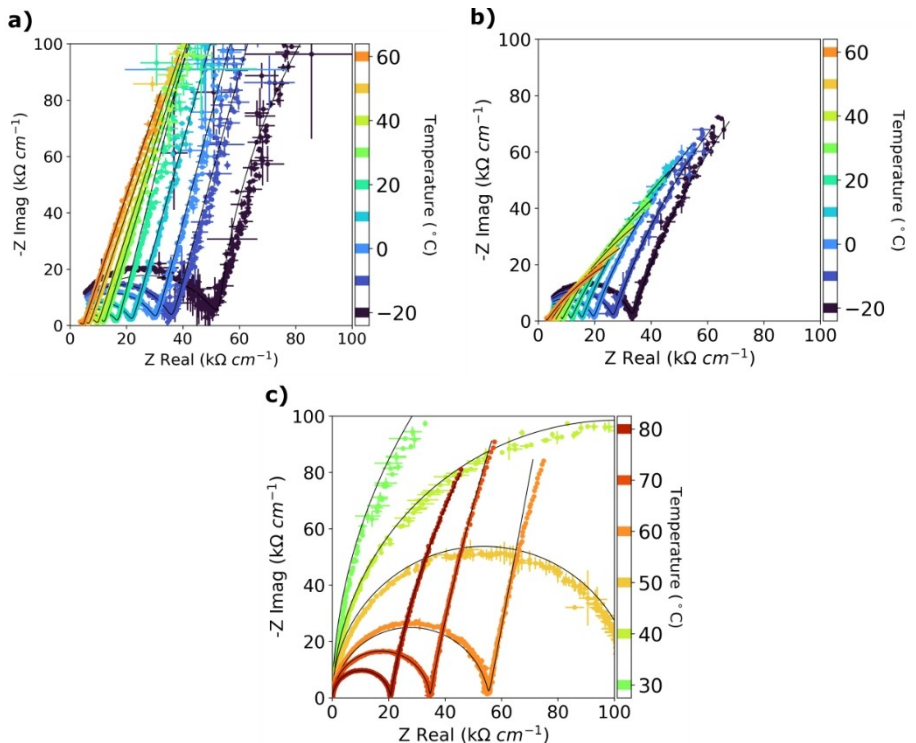


Figure 1. a) Nyquist plots showing temperature dependent EIS data for a composite of 10% polyIB and 90% LPSC by mass. b) Nyquist plots showing temperature dependent EIS data for a composite of 10% polyS and 90% LPSC by mass. c) Nyquist plots showing temperature dependent EIS data for the polyS material. All data are normalized by the thickness of the solid electrolyte layer. Equivalent circuit fits are shown as black lines. Data were collected at a cell stack-pressure of 1.6 MPa.

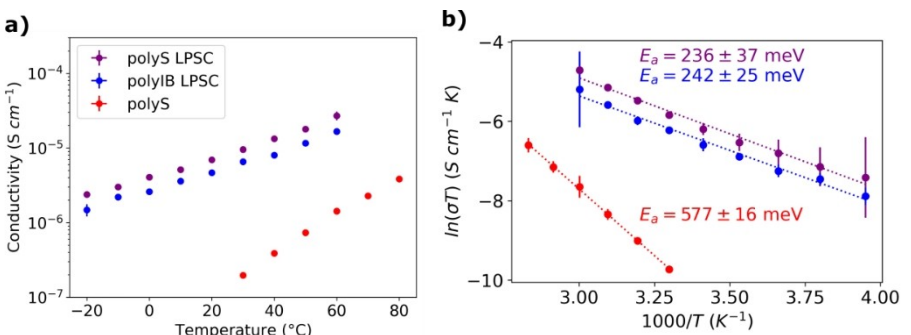
additive (10% by mass). The cells were assembled using indium electrodes pressed onto stainless steel rods and the data were collected using a custom-built Peltier cell system. At  $-20^{\circ}\text{C}$ , the data show an obvious semicircle in the approximately 1 MHz to 1 kHz frequency range. At frequencies lower than 1 kHz, a predominantly capacitive response is resolved. We attribute the semicircle to the mobility of  $\text{Li}^{+}$  ions across LPSC grains and within the bulk material. At temperatures approaching  $60^{\circ}\text{C}$ , the kinetics and the rate of bulk ionic diffusion are greatly accelerated, the ionic transport resistance decreases rapidly, and the semicircle becomes significantly smaller. Because of slight variations in material thickness, we note that all the data are normalized by the thickness of each respective solid electrolyte layer for direct comparison.

Figure 1(b) shows a series of analogous Nyquist plots depicting the temperature-dependent EIS data for a composite solid electrolyte layer comprised of LPSC argyrodite (90% by mass) and polyS (10% by mass). Across the range of temperatures, when compared to the data shown in Figure 1(a), the data in Figure 1(b) show smaller semicircles. The data in Figure 1(b) also show some non-capacitive (resistive) behavior at frequencies lower than 1 kHz. Specifically, in comparison to the spectra shown in Figure 1(a), the spectra in Figure 1(b) exhibit a pronounced non-vertical slope at frequencies below the semicircle inflection point and this slope decreases in angle with increasing temperature. We attribute this transport behavior to the relatively slow diffusion of semi-mobile organosulfide polymeric species with the addition of polyS to the composite. These species become increasingly mobile as the temperature increases, as evidenced by the gradual decrease in the low frequency slopes in the Nyquist spectra as the temperature is increased in the cell. Figure 1(c) shows a series of analogous Nyquist plots depicting the temperature-dependent EIS data for the standalone polyS material depicted in Scheme 1. The spectra show similar behavior to the spectra shown in Figures 1 and 2, where we posit that the semicircle represents temperature-dependent  $\text{Li}^{+}$  ion movement between polymer chains. We note that the polyS material exhibits very little ionic conductivity below  $30^{\circ}\text{C}$ . We therefore hypothesize that the predominant  $\text{Li}^{+}$  ion conduction mechanism in these polymers proceeds via an Li-S chain termination or an Li-amine site-

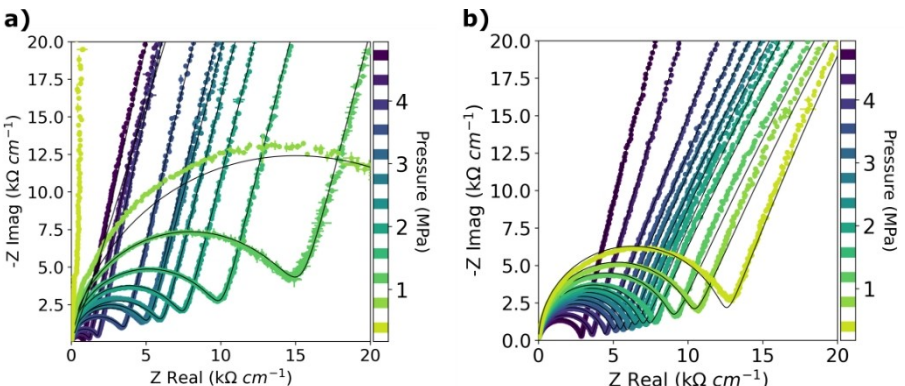
hopping mechanism, which is likely strongly temperature dependent and facilitated via the motion of the polysulfide chains.

Figure 2(a) shows the ionic conductivity values extracted from the Nyquist plots shown in Figure 1(a–c) by fitting the data to an equivalent circuit model (solid black lines shown in Figure 1). The polyS LPSC composite exhibits slightly higher ionic conductivities compared to the polyIB LPSC composite. When testing as a standalone solid electrolyte, the polyS material exhibits ionic conductivities in the range of  $10^{-6}$  S/cm at elevated temperatures ( $40$  to  $70^{\circ}\text{C}$ ), which is comparable to the measured ionic conductivities of other related polymers.<sup>[21,22]</sup> We note that the measured ionic conductivities of these composites are lower than what is typical for pure, highly densified LPSC pellets<sup>[7]</sup> because of the relatively high concentration of polymer (10% by mass) and very low stack-pressure (1.6 MPa) used in this study. Figure 2(b) shows the calculated activation energies for these three different materials, where the activation energies for the polyS LPSC and polyIB LPSC composites are approximately equal and the activation energy of the polyS material is calculated to be approximately 580 meV. Importantly, we note that in the case of the polyS LPSC composite, the introduction of an additional electrochemically active material interface does not drastically change the bulk material activation energy at 1.6 MPa, where both the polyS and polyIB data shown in Figure 2(b) demonstrate activation energies in the range of 240 meV. We hypothesize that if the LPSC interface were degraded by the introduction of the sulfur polymer, then this would result in an increase in the measured activation energy, which is not observed in Figure 2(b). Furthermore, the addition of the sulfur polymer increases the overall ionic conductivity of the composite, which is demonstrated by a systematic increase in the polyS versus polyIB data shown in Figure 2(a). Therefore, we conclude that the polyS material forms a stable, intimate interface with the LPSC particles without forming degraded surface species or an additional ionic conductivity bottleneck.

To further understand the enhanced ionic conductivity and stability of the polyS to LPSC interface, we conducted additional pressure-dependent EIS experiments. Figure 3(a) shows the Nyquist plots for the polyIB LPSC composite across a range of



**Figure 2.** a) Temperature dependent ionic conductivity for the PIB and LPSC composite (Nyquist data shown in Figure 1a), the polyS and LPSC composite (Nyquist data shown in Figure 1b), and the polyS material (Nyquist data shown in Figure 1c), and. b) Arrhenius plots and activation energies for the polyIB LPSC composite (Figure 1a, blue colored data), the polyS and LPSC composite (Figure 1b, purple colored data), and the polyS material (Figure 1c, red colored data), and. Data were collected at a cell stack-pressure of 1.6 MPa.



**Figure 3.** a) Nyquist plots showing pressure dependent EIS data for a composite of 10% polyIB and 90% LPSCl by mass. b) Nyquist plots showing pressure dependent EIS data for a composite of 10% polyS and 90% LPSCl by mass. The data are scaled by the thickness of the solid electrolyte layer and were collected at ambient temperature. Equivalent circuit fits are shown as black lines.

cell stack-pressure as measured using a custom designed pressure-dependent EIS system. At the lowest stack-pressure (0.4 MPa), the cell does not exhibit any measurable ionic conductivity and a purely capacitive response is measured, as indicated by a nearly vertical line on the Nyquist plot. As the cell stack-pressure is increased gradually to 4.7 MPa, the spectra exhibit an obvious semicircle in the approximately 1 MHz to 1 kHz frequency range. At frequencies lower than 1 kHz, a predominantly capacitive response is resolved. Like the temperature-dependent data shown in Figure 1, we attribute this semicircle to the mobility of  $\text{Li}^+$  ions across LPSC grains and within the bulk material. As the cell stack-pressure is increased, the LPSC particles have improved interfacial contact, an effective  $\text{Li}^+$  drift pathway under an electric field is increasingly likely to form, and the semicircle becomes significantly smaller. Figure 3(b) shows an analogous set of Nyquist plots for the polyS LPSC composite across the same range of cell stack-pressure. The spectra show an analogous transformation as the pressure increases, except that the semicircles in Figure 3(b) are significantly smaller at lower pressures (including at 0.4 MPa) when compared to that of Figure 3(a), thereby indicating higher  $\text{Li}^+$  conductivities at lower pressures for the polyS LPSC composite. We note that it is not possible to measure the ionic conductivity of polyS alone as a function of cell stack-pressure due to its highly flexible nature. Figure 4 compares the  $\text{Li}^+$  conductivities calculated by fitting the data using an equivalent circuit model. Importantly, we note that within the low-pressure region (grey highlighted area), the polyS LPSC composite exhibits higher ionic conductivities in comparison to the polyIB LPSC composite. At stack-pressure above 2.5 MPa, the polyIB LPSC composite begins to exhibit higher ionic conductivities in comparison to the polyS LPSC composite. We hypothesize that this is an effect of the level of interfacial contact between the LPSC particles in the composite as a function of pressure as depicted in Scheme 2. Specifically, at low pressures the highly flexible properties of the sulfur polymer improve interfacial contact between LPSC particles and effective ionic percolation pathways can be formed even if LPSC particles are not in direct contact with each other. Conversely, at low pressures the LPSC

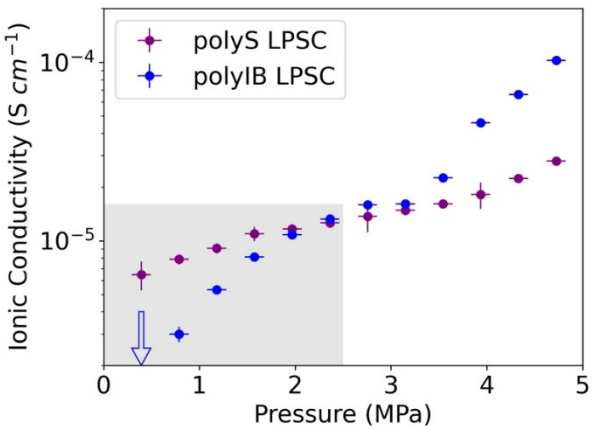
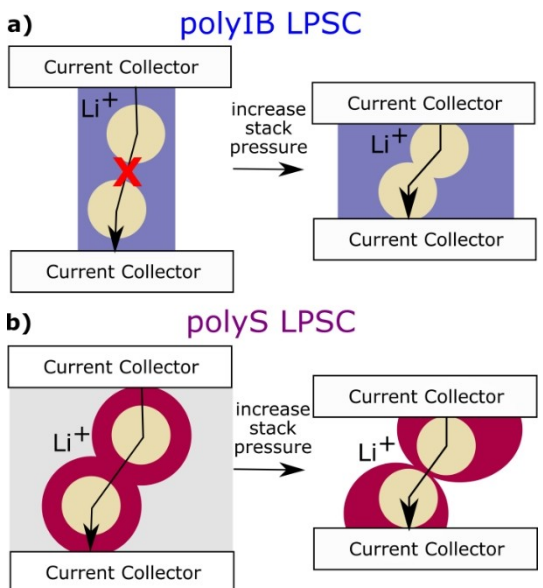


**Figure 4.** Ionic conductivity as a function of applied stack-pressure for the two different solid electrolyte composites. The low-pressure region where the polyS based composite exhibits improved ionic conductivity over the polyIB composite is highlighted with a grey box. The polyIB LPSC composite does not exhibit ionic conductivity ( $0 \text{ S cm}^{-1}$ ) at 0.4 MPa, as indicated by the blue arrow pointing at the independent axis.

particles in the polyIB LPSC composite are likely to be separated by a layer of non ionically conductive polyIB, which impedes ionic transport. At higher pressures, the LPSC particles begin to have improved interfacial contact, the ionic conductivity increases, and the chemically inert polyIB does not impede  $\text{Li}^+$  mobility between LPSC particles. In contrast, we posit that at higher pressures (approaching 5 MPa), in the case of the polyS LPSC composite, the polyS material remains chemically bound to the LPSC surface and adds an additional interface that limits the ultimate  $\text{Li}^+$  conductivity at higher pressures. These relationships are depicted and summarized in Scheme 2.

To better understand the mechanical properties of the polyS coated LPSC material, we examined the composite using atomic force microscopy (AFM) coupled with contact resonance (CR) measurements.<sup>[23]</sup> Figure 5(a) shows an elastic modulus map of composite material and a plot of the measured modulus along the dashed line in the map. Figure 5(b) shows the corresponding AFM surface morphology map of the composite simultaneously taken with the modulus map and a plot of the



**Scheme 2.** a) Illustration of polyIB LPSC composite interfacial contact as cell stack-pressure increases. b) Illustration of polyS LPSC composite with improved interfacial contact at low stack-pressures (highlighted in grey).

composite profile along the dashed line in the map.. The measured value is roughly consistent with the reported values of LPSC,<sup>[24,25]</sup> illustrating the dominance of the 90% LPSC in the overall elastic modulus. The data in Figure 5(a) suggest a domain structure where there are regions of relatively hard LPSC particles (light colors) surround by regions of the relatively mechanically soft polyS coating (dark colors), which is in agreement with our proposed core hypothesis as outlined in Scheme 2. The elastic modulus of composite materials is believed to be a collective effect in  $\sim\mu\text{m}$  scales, with a more weighted contribution in the local region together with

contributions from the surrounding regions.<sup>[26]</sup> Therefore, the smaller modulus of polyS-rich region is likely enhanced by the neighboring LPSC-dominated regions.

Using the discovery that the polyS material improves Li<sup>+</sup> transport at low pressures as a starting point, we fabricated a full solid-state cell using a lithium cobalt oxide (LCO) cathode, a graphite anode, and the LPSC polyS composite solid electrolyte. Figure 6 shows the EIS data collected during the initial cell lamination and densification step, where the full cell stack was pressed in a hydraulic press at a pressure of 760 MPa. At 760 MPa the Nyquist plot shows a typical Warburg diffusion response as indicated by the linear plot with a slope of approximately one. We attribute this behavior to the high level of intimate interfacial contact between the LPSC particles and the other electrode components at this comparatively high pressure. When this initial lamination pressure is relaxed to 1.6 MPa, the total impedance rises greatly as the LPSC particles lose some interfacial contact with their surrounding electrode components and neighboring LPSC grains. However, when the cell is subsequently heated from 25 °C to 70 °C, the cumulative absolute impedance of the cell drops down to levels commensurate with those seen at the initial lamination pressure of 760 MPa at 25 °C, albeit with a notably different spectrum shape due to the polyS-mediated Li<sup>+</sup> transport that occurs in the low-pressure regime. We attribute this significant increase in bulk ionic transport at low pressures and elevated temperatures to our core hypothesis that the polyS additive enhances interfacial contact of the LPSC particles as depicted in Scheme 2. Once the cell is heated slightly to 70 °C, the polysulfide chains begin moving and transporting Li<sup>+</sup> ions between LPSC grains that are no longer in intimate contact at low pressures. Next, we cycled this solid-state full cell at a nominal rate of C/20 with a 5 h voltage hold at top and bottom of charge. The voltage profiles for the first 6 cycles are shown in Figure 7(a). The specific capacity for the charge and discharge cycles as well as the

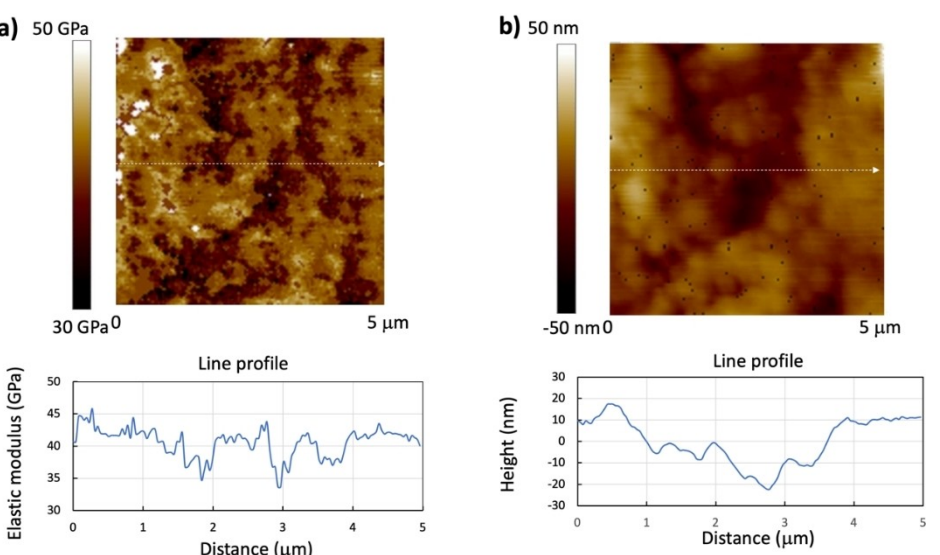


**Figure 5.** a) Contact resonance (CR) map of the polyS LPSC composite with a corresponding line scan. b) Atomic force microscopy (AFM) map of the same polyS LPSC composite region with corresponding line scan.

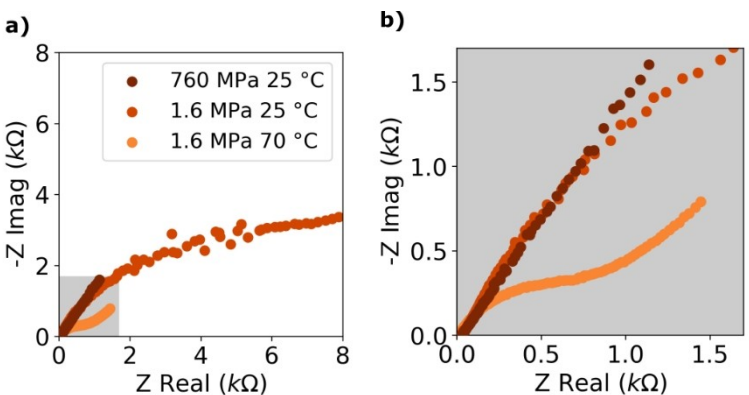


**Figure 6.** a) EIS data for a polyS LPSC composite LCO/Gr full cell initial lamination step in a hydraulic press at ambient temperature (760 MPa, 25 °C), in a low-pressure cell testing fixture at ambient temperature (1.6 MPa, 25 °C), and at 70 °C in the same low-pressure cell testing fixture (1.6 MPa, 70 °C). b) inset region of data are highlighted with a grey box.

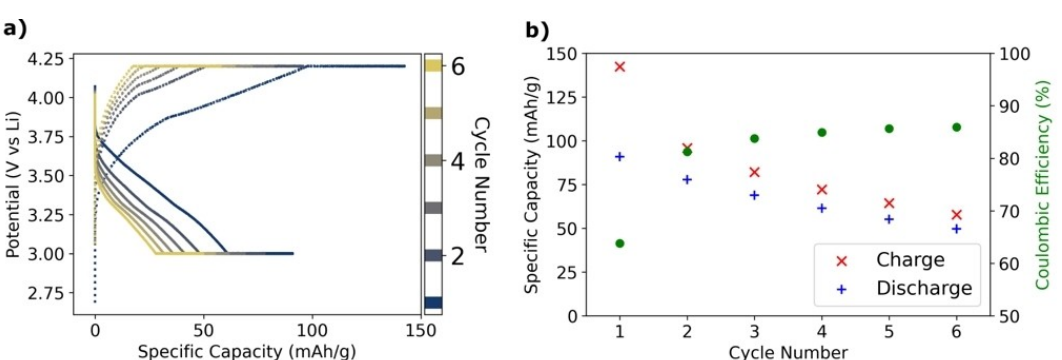


**Figure 7.** a) Voltage profiles for an LCO/graphite cell for 6 cycles with a C/5 nominal rate and a 5 h voltage hold at top and bottom of charge. The dotted lines represent the charge voltage profiles and the solid lines represent the discharge voltage profiles. b) Specific capacity and Coulombic efficiency for charge and discharge cycles normalized to the graphite mass with a cell N:P ratio of 1 and an areal capacity of 1.5 mAh/cm<sup>2</sup>. Data were collected at a cell stack-pressure of 1.6 MPa at 70 °C.

Coulombic efficiency are shown in Figure 7(b). We attribute the low irreversible capacity retention and low Coulombic efficiency of the full cell to the known interfacial redox degradation of LPSC, which is exacerbated in the presence of significant amounts of electrically conductive carbon additive (20% by mass in this study) and is not stable against high voltage cathodes without an additional passivation coating.<sup>[2,7,27–29]</sup> Importantly, we note that we were unable to fabricate an analogous cell with the polyIB binder for comparison that cycled reversibly at this low stack-pressure due to a very high impedance in the polyIB LPSC composite at cell stack-pressures below 2.0 MPa. These results further support our hypothesis that the flexible nature of the polyS interfacial coating is critical for fabricating low-pressure SSBs.

To better understand this LPSC redox degradation mechanism, to probe the lithium transport properties, and to study the surface chemistry evolution of the polyS LPSC composite, we also examined the composite using virtual electrode x-ray photoelectron spectroscopy (VE-XPS). VE-XPS is a technique which we have utilized previously to study other SSE materials.<sup>[9,30]</sup> VE-XPS experiments were performed on LPSC with (Figure 8) and without (Figure S2) the polyS additive. In these experiments, XPS measurements are performed while the

exposed sample surface is biased *in situ* via a low-energy electron source, which in turn drives bulk Li<sup>+</sup> migration toward the surface. On SSE materials, this approach enables direct observation of solid-electrolyte interphase (SEI) formation and evolution at the SSE/Li metal interface. The VE-XPS experimental data (presented in Figure 8) on the LPSC–polyS composite show that signals associated with the bulk material are almost completely attenuated by cycle 8, where a VE-XPS cycle denotes one period of lithiation using the low-energy electron flux, followed by acquisition of one set of XPS spectra. Note that the data set on LPSC (Figure S2) was acquired first, and the net electron fluence per cycle in that experiment was 3–4 times higher than the LPSC–polyS data set, and consequently the substrate signals attenuate proportionally faster. Based on a typical XPS information depth of ~10 nm, we can therefore estimate in this case that the net SEI thickness is approximately 10 nm at the point when Li plating initiates. The total amount of Li<sup>0</sup> needed to accomplish SEI formation and passivation can be estimated according to the expected decomposition pathway:



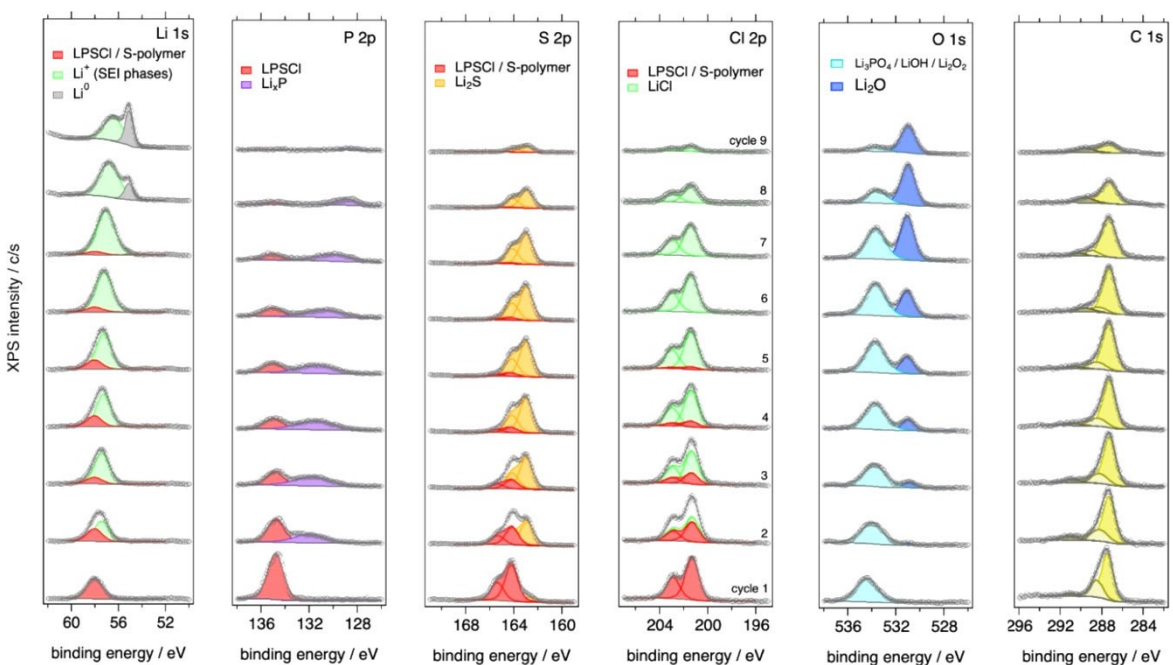


**Figure 8.** Selected spectra acquired during VE-XPS experiment on a polyS LPSC composite sample on lithium metal foil. These XPS core-level spectra reveal formation and passivation of the SEI (primarily comprised of  $\text{Li}_2\text{S}$ ,  $\text{Li}_3\text{P}$ ,  $\text{Li}_3\text{PO}_4$  and  $\text{Li}_2\text{O}$ ) followed by plating of metallic Li on the free surface. Each set of spectra represent one electron beam cycle, as indicated by the labels near the chlorine spectra.

Equation (1) does not consider oxygen-containing species, but nevertheless captures the primary decomposition pathways that have been predicted previously for SEI formation in this system,<sup>[31]</sup> and highlights that the amount of Li present in the SEI is about 133% higher than in the LPSC parent phase. We can further estimate that to form the passivated SEI for the LPSC–polyS sample requires an amount of  $\text{Li}^0$  equivalent to about 4 nm of metallic lithium.

Spectral decomposition of the XPS data sets were performed using self-consistent constraints in which binding energy separations and peak-area ratios were held constant for each phase.<sup>[9]</sup> The data shown in Figure 8 and Figure S2 reveal a conversion of LPSC into known subspecies for these materials, including  $\text{Li}_2\text{S}$ ,  $\text{Li}_x\text{P}$  ( $x \leq 3$ ) and  $\text{Li}_2\text{O}$  phases, followed by passivation of the interface and plating of metallic lithium on the exposed surface. No new chemical states were observed in the Cl 2p spectra, in contrast to the other LPSC elemental constituents. Nevertheless, since the Cl 2p peaks attenuate much more slowly than the bulk LPSC peak, we can infer that LiCl is likely a decomposition product that forms in the SEI. The spectral decomposition analysis reveals that the SEI phases are fully developed by approximately cycle 8, and the concomitant appearance of  $\text{Li}^0$  in the Li 1s spectrum indicates that the interface is passivated with respect to further SEI growth. Subsequently, the  $\text{Li}^0$  signal continues to grow, and the increasingly thick plated  $\text{Li}^0$  layer causes attenuation of SEI signals ( $\text{Li}_2\text{S}$  and  $\text{Li}_x\text{P}$ ). Previous studies revealed that  $\text{Li}_3\text{PO}_4$  and  $\text{Li}_2\text{O}$  phases might form in the SEI in cases where sufficient oxygen is present in the SSE material.<sup>[30]</sup> These and other potential O-containing phases are also observed here in the initial cycle of the VE-XPS experiment, although it should be

noted that the persistent O 1s signals at later stages of the experiment are likely at least partially due to reaction of the plated  $\text{Li}^0$  layer with residual gases present in the vacuum chamber. Overall, the polyS LPSC sample results (Figure 8) are analogous to those on the LPSC only sample (Figure S2). Two key differences when the polyS is included are the presence of a C 1s signal (as expected due to the DMVBA moieties) and a more prolonged  $\text{Li}_2\text{S}$  SEI formation, likely resulting from the partially mobile polyS sulfide (R–S–S–R) species reacting with  $\text{Li}^0$  to form  $\text{Li}_2\text{S}$  and R–S–Li species at the SEI.

To further probe this electrochemical interfacial reaction, we fabricated symmetric lithium metal electrode cells and cycled these galvanostatically using a polyS LPSC composite solid electrolyte layer. Figure 9 shows galvanostatic data for a Li/polyS LPSC/Li symmetric cell with 1 h galvanostatic pulses at a  $\sim 100 \mu\text{A}/\text{cm}^2$  current density. Figure 9(a) shows the time window during which the first initial EIS spectra were collected before testing (green rectangle, t1), followed by one galvanostatic cycle and the window for the second EIS spectra collection (second green rectangle, t2). The data in Figure 9(b) show the voltage response for 6 additional galvanostatic cycles followed by an additional EIS spectra collection time window (grey rectangle, t3). The voltage response in Figure 9(b) decreases in comparison to Figure 9(a) and fluctuates during the galvanostatic holds until it is only a few mV at approximately 15 h prior to the third EIS collection window (t3). Figure 9(c) shows the voltage response during an additional 11 cycles, which gradually increases and fluctuates until before the fourth EIS collection window (green rectangle, t4) to approximately 200 mV at approximately 15 h, which is commensurate with the initial voltage response shown in Figure 9(a). Fig-

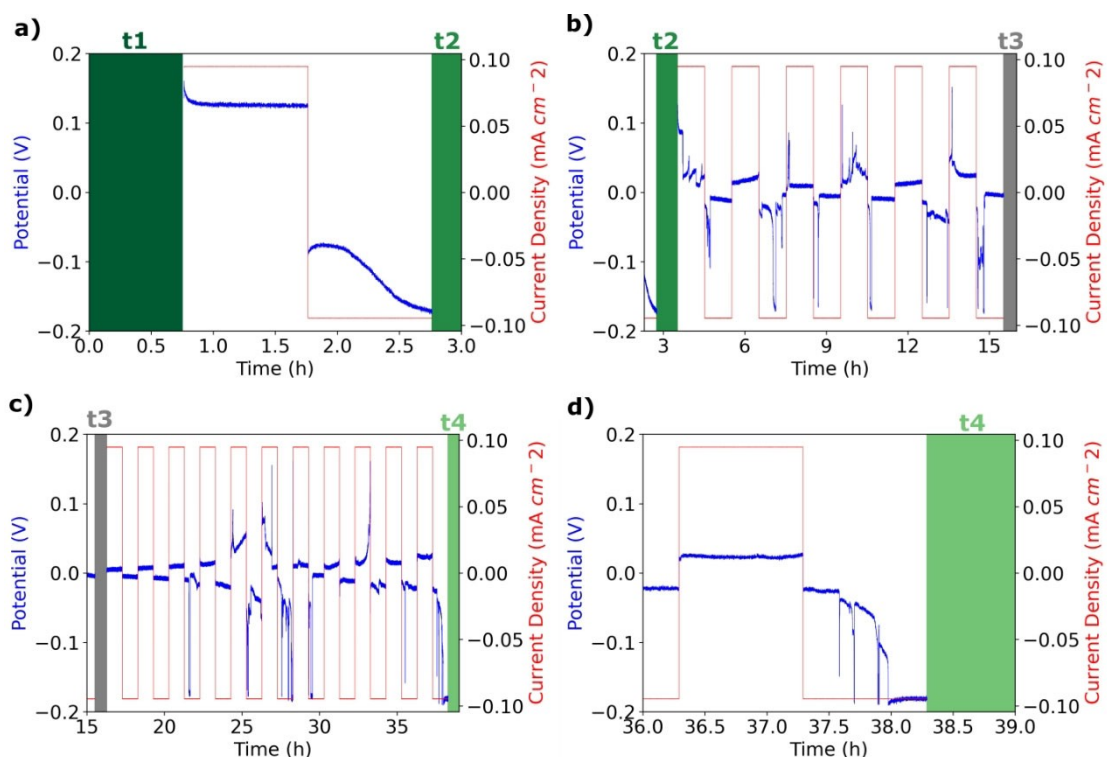
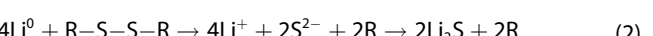


**Figure 9.** Sequential (a, b, c, and d) 1 h galvanostatic pulses of a Li/Li symmetric cell polyS LPSC composite at 60°C and 1.6 MPa. The grey colored line at 15.5 h (t3) indicates when cell shorting was detected via EIS. The green colored lines indicate times when EIS spectra were collected without cell shorting at 0 h (t1), 2.8 h (t2), and 38.3 h (t4).

ure 9(d) shows the zoomed in region where the voltage response is increasing leading up to the t4 EIS data collection window. Figure 10 shows the Nyquist plots for the EIS data collected during t1, t2, t3, and t4.

We posit that this electrochemical behavior can be explained by the mobility of the polyS species at elevated temperatures. The EIS data in Figure 1 indicate that the polyS material likely imbues the composite with a flux of relatively

kinetically slow, partially mobile organosulfide species. Furthermore, the spectra shown in Figure 8 indicate that a dynamic SEI at the lithium metal interface is likely comprised mainly of Li<sub>2</sub>S-like species. Therefore, we posit that after some period of galvanostatic cycling the cell becomes shorted from the formation of lithium metal dendrites. During subsequent cycles, the partially mobile organosulfide species (R—S—S—R) oxidize the Li<sup>0</sup> dendrites to form temporarily passivating Li<sub>2</sub>S-like species via some variation of the simplified reaction mechanism:



This proposed self-healing dynamic is represented graphically in Scheme 3. We observed no such self-healing mechanism in Li/LPSC/Li cells that do not contain any polyS, thereby indicating that the extra R—S—S—R mobility from the polyS is essential for this mechanism. Previous studies have reported similar self-healing behavior for organosulfide coatings in lithium-anode liquid electrolyte cells.<sup>[32,33]</sup>

## Conclusions

We have developed a novel sulfur polymer that can be combined with Li<sub>6</sub>PS<sub>5</sub>Cl (LPSC) argyrodite to form a new solid electrolyte (SE) composite. By creating this new SE composite, we combined the LPSC particles with a flexible, ionically conductive interfacial additive that maintains the low activation

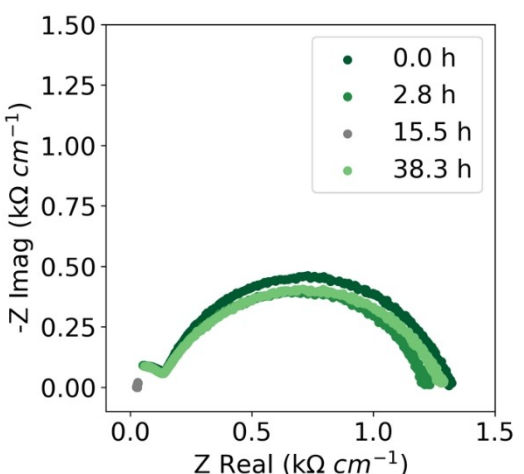
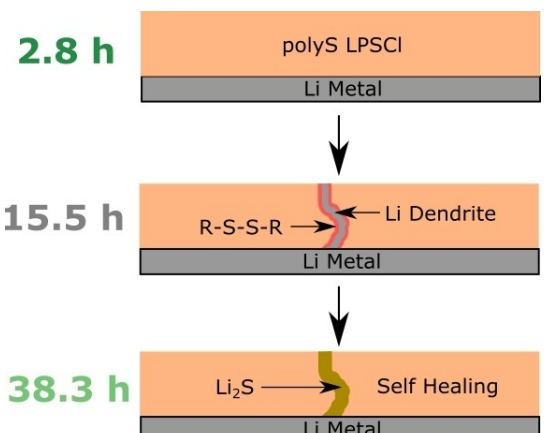


**Figure 10.** EIS data collected at times indicated by the vertical lines shown in Figure 9. The grey colored dataset at 15.5 h indicates when cell shorting was detected (0 Ω impedance).



**Scheme 3.** Scheme depicting self-healing mechanism wherein the polyS LPSC composite promotes organosulfide ( $R-S-S-R$ ) flux-mediated oxidation of  $Li^0$  dendrites to  $Li_2S$  compounds.

energies for lithium-ion mobility in LPSC. Moreover, we showed that the addition of polyS significantly increases ionic conductivities at cell stackpressures below 2 MPa. Furthermore, we demonstrated that this new composite SE can be utilized to fabricate effective solid-state batteries (SSBs) that can reversibly cycle at a cell stack-pressure of only 1.6 MPa. We also conducted atomic force microscopy-based contact resonance (AFM-CR) to illustrate the soft and flexible nature of the polyS as an interfacial SE additive. We analyzed the dynamic interfacial evolution of the polyS LPSC composite using virtual electrode x-ray photoelectron spectroscopy (VE-XPS). The VE-XPS data show that the polyS LPSC composite forms a  $Li_2S$  rich solid-electrolyte interphase (SEI) prior to lithium plating. This novel sulfur polymer also demonstrates self-healing properties when combined with a lithium metal electrode. Specifically, once a lithium metal dendrite forms and a cell is shorted, based on the VE-XPS data, we posit that the mobile organosulfide species in the sulfur polymer can oxidize the lithium metal dendrite to form a passivating lithium sulfide material and the cell is no longer shorted.

## Experimental

All reagents and solvents were purchased from Sigma Aldrich and used as received unless otherwise noted.

### Sulfur polymer synthesis

1 g of elemental sulfur was placed in a sealed flask and was degassed and purged under dry nitrogen on a vacuum gas manifold system. The sulfur was heated to 130 °C until a yellow liquid was formed indicating the formation of linear sulfur diradicals. 2.7 mL of dimethylvinylbenzylamine (DMVBA) was injected into the liquid sulfur. The temperature was increased to 180 °C and the polymerization was conducted for 60 min, until a dark red liquid formed. The reaction was quenched by cooling to ambient temperature. The nominal stoichiometric ratio of sulfur atoms to DMVBA molecules was 2 to 1.

Next, 500 mg of this polymer was dissolved in 10 mL of distilled and dehydrated *n*-methyl-2-pyrrolidone (NMP) with stirring in a glass vial with an integrated septum cap inside of an argon filled glovebox. 188 mg of LiCl was added to this solution and an 18-gauge needle was inserted through the septum to limit NMP vapor flux and mitigate solvent bubbling. The glass vial was placed inside of a sealed glass vacuum chamber and the mixture was heated to 200 °C and placed under vacuum (several mTorr) with stirring. The polymer lithiation reaction proceeded for 120 min to produce a green colored solution. During this time, the polymer was also slowly dried as the NMP evaporated through the needle. The resulting dried, lithiated sulfur polymer was used without further purification.

### $Li_6PS_5Cl$ (LPSC) composite formation

For the polyS LPSC composite, 20 mg of polyS was dissolved in 10 mL of anhydrous toluene in a glass vial with stirring. 180 mg of  $Li_6PS_5Cl$  (LPSC, fine powder, MSE supplies) was added to this solution. The glass vial was placed inside of a sealed glass vacuum chamber and the mixture was heated to 100 °C and placed under vacuum (several mTorr) for 30 min until dried.

For the polyisobutene composite, an analogous procedure was used, except the LPSC was combined with 20 mg of dissolved polyIB (BASF, Oppanol) instead of polyS and dried, where the polyIB was dissolved for 24 h in anhydrous toluene with stirring at ambient temperature.

### Electrochemical impedance spectroscopy (EIS)

EIS measurements were performed on a Biologic VMP3 potentiostat across a frequency range of 1 MHz to 1 Hz with a perturbation amplitude of 30 mV. Each spectrum was produced by averaging the response of three separate scans, where the first scan was performed from high to low frequencies, the second scan was performed from low to high frequencies, and the third and final scan was performed from high to low frequencies. These three spectra were examined for any systematic variations in response, where consistent differences in these scans would indicate a potential nonlinear response or a non-equilibrium electrochemical state in the cell. The final spectrum was produced by averaging the three scans together and the error bars in the Nyquist plots represent one standard deviation in the data. The spectra were fit to an equivalent circuit model consisting of a resistor in parallel with a constant phase element (bulk ionic conductivity response) combined in series with a second resistor in parallel with a constant phase element (electrode interfacial response).

### Temperature-dependent ionic conductivity measurements

All cell assembly was performed inside of an argon filled glovebox. 200 mg of polyS LPSC composite, or polyIB LPSC composite was placed on top of a 12.7 mm diameter punch of indium metal foil (0.1 mm thick) inside of a custom-built polyether ether ketone (PEEK) cell housing with stainless steel contact rods (cell system shown in Figure S6). A second indium metal foil electrode was placed on top of the polyS and the cell was sealed against atmosphere, removed from the glovebox, and placed in a custom-built, cell-stack spring pressurization system. The resulting cell was then placed inside of a custom-built Peltier heating and cooling system. For each temperature step, the cell was allowed to equilibrate for 2 h prior to spectral analysis. The cell was analyzed using the EIS methods described above.

### Pressure-dependent ionic conductivity measurements

A symmetric In/LPSC composite/In PEEK cell was fabricated using the same methods described above. The cell was placed inside of a custom-built, spring pressurization system with a uniaxial load cell to continuously monitor cell stack-pressure (cell system shown in Figure S6). The cell stack-pressure was varied by systematically compressing the springs in the system to a specific force value.

### Lithium cobalt oxide (LCO) cathode and graphite anode solid-state battery (SSB) assembly

The cathode powder was fabricated by combining 60 mg of LCO (Targray) with 100 mg of polyS LPSC composite (10% polyS by mass) and 40 mg of vapor grown carbon fiber nanorods (VGCF) by hand in a mortar and pestle in an argon filled glovebox. The anode powder was formed by using an analogous method, except that the 60 mg of LCO was substituted for 60 mg of graphite.

To form the full SSB, each layer of the cell was assembled via a stepwise lamination procedure. First, 15 mg of anode powder was placed on top of a titanium current collector rod inside of a custom-built, high-pressure PEEK cell system (cell system shown in Figure S6). This anode electrode layer was densified into a pellet using a hydraulic press inside of an argon filled glovebox by pressing the powder at 150 MPa. Next, 50 mg of LPSC powder was placed on top of the anode layer and was subsequently pressed at 150 MPa. Finally, 20 mg of the cathode powder (~1.0 N to P ratio, 1.5 mAh/cm<sup>2</sup>) was placed on top of the LPSC separator layer and the final cell was pressed at 760 MPa in the hydraulic press.

The cell was examined using EIS, removed from the hydraulic press, sealed, removed from the glovebox, and placed in a custom-built spring pressurization jig at a stack-pressure of 1.6 MPa. The cell was heated to 70 °C for 2 h inside of a laboratory oven until temperature equilibration and was examined using EIS. The cell was then cycled at a nominal C/5 rate (100 µA/cm<sup>2</sup>) using a Biologic VMP3 potentiostat.

### Atomic force microscopy (AFM)-based contact resonance (CR)

CR was performed using the peak force (PF) mode of an AFM (BrukerNano, Dimension Icon and NanoScope V) with a diamond coated Si probe (BrukerNano, DDLTESP). CR measures the resonant oscillation of probe/sample contact by sweeping the oscillation frequency in 100k-1200k Hz range. A higher/lower resonant frequency corresponds to a higher/lower elastic modulus of the sample. The sample was mechanically oscillated, and the oscillation of probe was measured during the period of probe/sample contact in the PF-AFM mode. The probe spring constant and AFM instrumental cantilever deflection sensitivity were determined by reference thermal tune and force-distance curves, where the latter was measured by contacting the probe on a sample. The important parameters of probe size and the probe location on the rectangular probe cantilever were calibrated by using reference samples of Al, Si, and Cr with well-known modulus values. Each CR-image has 128×128 pixels of data.

### Virtual electrode X-ray photoelectron spectroscopy (VE-XPS)

Lithium metal electrodes were fabricated by pressing a 6 mm diameter punch of 0.7 mm thick lithium metal onto a 12.7 mm diameter punch of 0.1 mm thick stainless steel foil until a flat mirror finish was achieved. Next, 200 mg of polyS LPSC composite was densified into a pellet (12.7 mm diameter) in a hydraulic press. This pellet was then pressed onto the lithium metal electrode. VE-XPS

measurements were performed in a Physical Electronics Phi VersaProbe III instrument using Al- $\text{K}\alpha$  excitation ( $h\nu = 1486.7 \text{ eV}$ ). Binding energies were calibrated using Cu 2p<sub>3/2</sub> (932.62 eV) and Au 4f<sub>7/2</sub> (83.96 eV) core level spectra acquired from sputter-cleaned foils. Electron bias current was supplied by an electron gun source operated at an incident kinetic energy of 10 eV, and an estimated current density of 28 µA/cm<sup>2</sup> based on calibration measurements using a Faraday cup. Assuming one Li<sup>+</sup> ion is transported to the surface for each electron, we estimate an equivalent of two monolayers of metallic Li is brought to the surface during each 10 s exposure per cycle under these conditions.

### Lithium metal symmetric cell

Lithium metal electrodes were fabricated using the same procedure described above. Next, 200 mg of polyS LPSC composite was placed on top of the lithium metal electrode inside of a custom-built PEEK cell housing with stainless steel contact rods. A second lithium metal electrode was placed on top of the polyS LPSC composite and the cell was sealed against atmosphere, removed from the glovebox, and placed in a custom-built, cell-stack spring pressurization system. The resulting cell was then placed inside of a custom-built Peltier heating and cooling system and was heated to 70 °C for 2 h until temperature equilibration. The cell was then galvanostatically cycled at current density of 100 µA/cm<sup>2</sup> with 1 h pulses and intermittent EIS analysis using a Biologic VMP3 potentiostat.

### Fourier transform infrared spectroscopy (FTIR)

FTIR spectra were collected with a ThermoFisher Nicolet 7600 using a liquid nitrogen cooled MCT-A detector and a Smart iTx diamond attenuated total reflection (ATR) attachment. A custom airtight PEEK enclosure was constructed and used to perform the experiment. For the sulfur polymer spectra, a small amount (~5 mg) of sulfur polymer was pressed directly onto the diamond crystal inside of a glovebox and the system was sealed with Kalrez O-rings to keep the sample air-free. For the DMVBA sample, a small amount (~500 µL) of monomer was pipetted onto the diamond crystal and the system was sealed with Kalrez O-rings in ambient atmosphere.

### <sup>1</sup>H nuclear magnetic resonance (NMR) spectroscopy

All samples were tested in CDCl<sub>3</sub> solvent at approximately a 10 mg per mL concentration. <sup>1</sup>H NMR spectra were acquired at 25 °C on a Bruker Avance NeoNanobay 300 MHz spectrometer at 7.05 T using a room temperature broadband probe. Spectra were acquired with a spectral width of 14 ppm with a recycle delay of 1 s and 8 scans. All spectral processing was done in Bruker Topspin version 3.6.1. DMVBA was used as received without drying or further purification. NMR tubes were dried overnight in an oven at 100 °C prior to use.

### Supporting Information

Supporting Information includes additional spectroscopic characterizations of the sulfur polymer, VE-XPS data and XPS analysis of the polyS material, and images of custom cell testing equipment. The authors have cited additional references within the Supporting Information.<sup>[34–36]</sup>

## Acknowledgements

This work was authored in part by the National Renewable Energy Laboratory (NREL), operated by Alliance for Sustainable Energy, LLC, for the U.S. Department of Energy (DOE) under Contract No. DE-AC36-08GO28308. Funding provided by the U.S. Department of Energy's Vehicle Technologies Office (VTO) under the Low-Pressure All-Solid-State Cells project directed by Simon Thompson and Tien Duong and managed by Anthony Burrell. The views expressed in the article do not necessarily represent the views of the DOE or the U.S. Government. The U.S. Government retains and the publisher, by accepting the article for publication, acknowledges that the U.S. Government retains a nonexclusive, paid-up, irrevocable, worldwide license to publish or reproduce the published form of this work, or allow others to do so, for U.S. Government purposes.

## Conflict of Interests

The authors declare no competing financial interests.

## Data Availability Statement

The data that support the findings of this study are available from the corresponding author upon reasonable request.

**Keywords:** ion-conducting polymers • lithium anodes • lithium-ion batteries • solid-state batteries • solid electrolytes

- [1] L. Ye, X. Li, *Nature* **2021**, *593*, 218.
- [2] D. H. S. Tan, Y. T. Chen, H. Yang, W. Bao, B. Sreenarayanan, J. M. Doux, W. Li, B. Lu, S. Y. Ham, B. Sayahpour, J. Scharf, E. A. Wu, G. Deysher, H. E. Han, H. J. Hah, H. Jeong, J. B. Lee, Z. Chen, Y. S. Meng, *Science* **2021**, *373*, 1494.
- [3] T. A. Yersak, C. Stoldt, S.-H. Lee, *J. Electrochem. Soc.* **2013**, *160*, A1009.
- [4] A. Kondori, M. Esmaeilirad, A. M. Harzandi, R. Amine, M. T. Saray, L. Yu, T. Liu, J. Wen, N. Shan, H. H. Wang, A. T. Ngo, P. C. Redfern, C. S. Johnson, K. Amine, R. Shahbazian-Yassar, L. A. Curtiss, M. Asadi, *Science* **2023**, *379*, 499.
- [5] R. Chen, Q. Li, X. Yu, L. Chen, H. Li, *Chem. Rev.* **2020**, *120*, 6820.
- [6] J. C. Bachman, S. Muy, A. Grimaud, H. H. Chang, N. Pour, S. F. Lux, O. Paschos, F. Maglia, S. Lupart, P. Lamp, L. Giordano, Y. Shao-Horn, *Chem. Rev.* **2016**, *116*, 140.
- [7] Y. Xiao, Y. Wang, S. H. Bo, J. C. Kim, L. J. Miara, G. Ceder, *Nat. Rev. Mater.* **2020**, *5*, 105.
- [8] S. Chen, D. Xie, G. Liu, J. P. Mwizerwa, Q. Zhang, Y. Zhao, X. Xu, X. Yao, *Energy Storage Mater.* **2018**, *14*, 58.
- [9] A. L. Davis, E. Kazyak, J. Sakamoto, N. P. Dasgupta, R. Garcia-Mendez, K. H. Chen, K. N. Wood, G. Teeter, K. N. Wood, *J. Mater. Chem. A* **2020**, *8*, 6291.
- [10] Q. Zhao, S. Stalin, C. Z. Zhao, L. A. Archer, *Nat. Rev. Mater.* **2020**, *5*, 229.
- [11] W. J. Chung, J. J. Griebel, E. T. Kim, H. Yoon, A. G. Simmonds, H. J. Ji, P. T. Dirlam, R. S. Glass, J. J. Wie, N. A. Nguyen, B. W. Guralnick, J. Park, Á. Somogyi, P. Theato, M. E. Mackay, Y.-E. Sung, K. Char, J. Pyun, *Nat. Chem.* **2013**, *5*, 518.
- [12] P. T. Dirlam, J. Park, A. G. Simmonds, K. Domanik, C. B. Arrington, J. L. Schaefer, V. P. Oleshko, T. S. Kleine, K. Char, R. S. Glass, C. L. Soles, C. Kim, N. Pinna, Y. Sung, *ACS Appl. Mater. Interfaces* **2016**, *8*, 13437.
- [13] Y. Zhang, R. S. Glass, K. Char, J. Pyun, *Polym. Chem.* **2019**, *10*, 4078.
- [14] T. R. Martin, K. A. Mazzio, H. W. Hillhouse, C. K. Luscombe, *Chem. Commun.* **2015**, *51*, 11244.
- [15] A. G. Simmonds, J. J. Griebel, J. Park, K. R. Kim, W. J. Chung, V. P. Oleshko, J. Kim, E. T. Kim, R. S. Glass, C. L. Soles, Y.-E. Sung, K. Char, J. Pyun, *ACS Macro Lett.* **2014**, *3*, 229.
- [16] Y. Zhang, J. J. Griebel, P. T. Dirlam, N. A. Nguyen, R. S. Glass, M. E. Mackay, K. Char, J. Pyun, *J. Polym. Sci. Part A* **2017**, *55*, 107.
- [17] T. S. Kleine, N. A. Nguyen, L. E. Anderson, S. Namnabat, E. A. Lavilla, S. A. Showghi, P. T. Dirlam, C. B. Arrington, M. S. Manchester, J. Schwiegerling, R. S. Glass, K. Char, R. A. Norwood, M. E. Mackay, J. Pyun, *ACS Macro Lett.* **2016**, *5*, 1152.
- [18] D. A. Boyd, V. Q. Nguyen, C. C. McClain, F. H. Kung, C. C. Baker, J. D. Myers, M. P. Hunt, W. Kim, J. S. Sanghera, *ACS Macro Lett.* **2019**, *8*, 113.
- [19] D. H. S. Tan, A. Banerjee, Z. Deng, E. A. Wu, H. Nguyen, J. M. Doux, X. Wang, J. H. Cheng, S. P. Ong, Y. S. Meng, Z. Chen, *ACS Appl. Energ. Mater.* **2019**, *2*, 6542.
- [20] N. Riphaus, P. Strobl, B. Stiaszny, T. Zinkevich, M. Yavuz, J. Schnell, S. Idris, H. A. Gasteiger, S. J. Sedlmaier, *J. Electrochem. Soc.* **2018**, *165*, A3993.
- [21] I. Gomez, A. F. De Anastro, O. Leonet, J. A. Blazquez, H. J. Grande, J. Pyun, D. Mecerreyes, *Macromol. Rapid Commun.* **2018**, *39*, 1.
- [22] Y. Jiang, X. Yan, Z. Ma, P. Mei, W. Xiao, Q. You, Y. Zhang, *Polymers (Basel)* **2018**, *10*, 1.
- [23] P. A. Yuya, D. C. Hurley, J. A. Turner, *J. Appl. Phys.* **2008**, *104*, 074916.
- [24] Z. Deng, Z. Wang, I.-H. Chu, J. Luo, S. P. Ong, *J. Electrochem. Soc.* **2016**, *163*, A67.
- [25] R. Garcia-Mendez, J. G. Smith, J. C. Neufeld, D. J. Siegel, J. Sakamoto, *Adv. Energy Mater.* **2020**, *10*, 1.
- [26] M. B. Dixit, W. Zaman, N. Hortance, S. Vujic, B. Harkey, F. Shen, W. Y. Tsai, V. De Andrade, X. C. Chen, N. Balke, K. B. Hatzell, *Joule* **2020**, *4*, 207.
- [27] A. Banerjee, H. Tang, X. Wang, J. H. Cheng, H. Nguyen, M. Zhang, D. H. S. Tan, T. A. Wynn, E. A. Wu, J. M. Doux, T. Wu, L. Ma, G. E. Sterbinsky, M. S. D'Souza, S. P. Ong, Y. S. Meng, *ACS Appl. Mater. Interfaces* **2019**, *11*, 43138.
- [28] D. H. S. Tan, E. A. Wu, H. Nguyen, Z. Chen, M. A. T. Marple, J. M. Doux, X. Wang, H. Yang, A. Banerjee, Y. S. Meng, *ACS Energy Lett.* **2019**, *4*, 2418.
- [29] X. Chen, X. Li, L. Luo, S. He, J. Chen, Y. Liu, H. Pan, Y. Song, R. Hu, *Adv. Energy Mater.* **2023**, *2301230*, 1.
- [30] K. N. Wood, K. X. Steirer, S. E. Hafner, C. Ban, S. Santhanagopalan, S. H. Lee, G. Teeter, *Nat. Commun.* **2018**, *9*, 1.
- [31] Y. Zhu, X. He, Y. Mo, *ACS Appl. Mater. Interfaces* **2015**, *7*, 23685.
- [32] G. Li, Y. Gao, X. He, Q. Huang, S. Chen, S. H. Kim, D. Wang, *Nat. Commun.* **2017**, *8*, 850.
- [33] D. Wang, G. Li, Q. Huang, X. He, Y. Gao, D. Wang, S. H. Kim, *ACS Nano* **2018**, *12*, 1500.
- [34] N. Saqib, G. M. Ohlhausen, J. M. Porter, *J. Power Sources* **2017**, *364*, 266.
- [35] A. Rafie, R. Pereira, A. A. Shamsabadi, V. Kalra, *J. Phys. Chem. C* **2022**, *126*, 12327.
- [36] T. Yu, F. Li, C. Liu, S. Zhang, H. Xu, G. Yang, *J. Mater. Chem. A* **2017**, *5*, 9293.

Manuscript received: July 19, 2023  
Revised manuscript received: August 15, 2023  
Accepted manuscript online: August 17, 2023  
Version of record online: August 29, 2023